Surface Science 646 (2016) 210–220

Contents lists available at ScienceDirect

Surface Science

journal homepage: www.elsevier.com/locate/susc

CO adsorption over Pd nanoparticles: A general framework for IR simulations on nanoparticles

Constantinos D. Zeinalipour-Yazdi [a,b,*], David J. Willock [a,**], Liam Thomas [a], Karen Wilson [c], Adam F. Lee [c,***]

[a] Cardiff Catalysis Institute, Cardiff University, Park Place, Cardiff CF10 3AT, UK
[b] Department of Chemistry, University College London, London WC1H 0AJ, UK
[c] European Bioenergy Research Institute, Aston University, Birmingham B4 7ET, UK

ARTICLE INFO

Available online 18 July 2015

Keywords:
Palladium
Nanoparticles
Carbon monoxide
Density functional theory
Chemisorption
IR spectroscopy

ABSTRACT

CO vibrational spectra over catalytic nanoparticles under high coverages/pressures are discussed from a DFT perspective. Hybrid B3LYP and PBE DFT calculations of CO chemisorbed over Pd_4 and Pd_{13} nanoclusters, and a 1.1 nm Pd_{38} nanoparticle, have been performed in order to simulate the corresponding coverage dependent infrared (IR) absorption spectra, and hence provide a quantitative foundation for the interpretation of experimental IR spectra of CO over Pd nanocatalysts. B3LYP simulated IR intensities are used to quantify site occupation numbers through comparison with experimental DRIFTS spectra, allowing an atomistic model of CO surface coverage to be created. DFT adsorption energetics for low CO coverage ($\theta \rightarrow 0$) suggest the CO binding strength follows the order hollow > bridge > linear, even for dispersion-corrected functionals for sub-nanometre Pd nanoclusters. For a Pd_{38} nanoparticle, hollow and bridge-bound are energetically similar (hollow ≈ bridge > atop). It is well known that this ordering has not been found at the high coverages used experimentally, wherein atop CO has a much higher population than observed over Pd(111), confirmed by our DRIFTS spectra for Pd nanoparticles supported on a KIT-6 silica, and hence site populations were calculated through a comparison of DFT and spectroscopic data. At high CO coverage ($\theta = 1$), all three adsorbed CO species co-exist on Pd_{38}, and their interdiffusion is thermally feasible at STP. Under such high surface coverages, DFT predicts that bridge-bound CO chains are thermodynamically stable and isoenergetic to an entirely hollow bound Pd/CO system. The Pd_{38} nanoparticle undergoes a linear (3.5%), isotropic expansion with increasing CO coverage, accompanied by 63 and 30 cm^{-1} blue-shifts of hollow and linear bound CO respectively.

© 2015 Elsevier B.V. All rights reserved.

1. Introduction

CO adsorption and activation over platinum group metals (PGMs, i.e. Pt, Ir, Ru, Rh, and Pd) [1] are key steps in some of the world's most important catalytic processes [2,3]. Early surface science studies by Ertl and co-workers shed valuable light on CO adsorption/oxidation (i.e. $CO + ½O_2 \rightarrow CO_2$) on palladium surfaces, evidencing a competitive Langmuir–Hinshelwood mechanism [4–8]. Nowadays, palladium is a key component of automotive emission control three-way catalysts (TWCs) for gasoline vehicles, facilitating low temperature oxidation [9]. Supported PGMs have also shown outstanding low temperature performance for the water-gas shift (WGS) reaction (i.e. $CO + H_2O \rightarrow CO_2 + H_2$)[10], the electrochemical oxidation of CO [11], and CO methanation in which CO coverage-dependent rate changes of 2–3 orders of magnitude have been recently observed [12]. These important processes place a heavy demand on the supply of these costly and scarce elements. To mitigate the cost and improve the sustainability of PGM catalysts, academic and industrial researchers seek more efficient catalyst designs, such as supported nanoparticles (NPs), which offer very high surface area to volume ratios for the active metal component, or alloying with a non-noble metal to minimise the precious metal content and tailor its electronic properties [13]. A strong NP/support interaction is also desirable to hinder particle sintering and attendant loss of active surface area.

In addition to its roles in pollution control and chemical synthesis, CO is also widely employed in heterogeneous catalysis as a strongly-interacting probe molecule for evaluating the dispersion and morphology of PGM nanoparticles via thermal desorption and/or vibrational spectroscopies [14,15]. However, the correct interpretation of resulting experimental spectra is critically dependent upon a quantitative understanding of factors influencing the observed CO stretching frequency, which to date has only been derived via surface science experiments over well-defined single crystal surfaces. For nanoparticulate catalysts such as CO stretching frequencies are anticipated to be sensitive to NP size, the exposed facets, support interactions, and coverage dependent (substrate-mediated or direct) lateral interactions between

* Corresponding author.
** Corresponding author.
*** Corresponding author at: European Bioenergy Research Institute, Aston University, Birmingham B4 7ET, UK.
E-mail addresses: c.zeinalipour-yazdi@ucl.ac.uk (C.D. Zeinalipour-Yazdi), WillockDJ@cardiff.ac.uk (D.J. Willock), A.F.Lee@aston.ac.uk (A.F. Lee).

http://dx.doi.org/10.1016/j.susc.2015.07.014
0039-6028/© 2015 Elsevier B.V. All rights reserved.

co-adsorbed CO molecules [16]: these effects are extremely difficult to probe independently through experiment. Density functional theory (DFT) calculations offer a powerful methodology by which to estimate the energetic, structural and spectroscopic properties of CO over free and supported transition and noble metal clusters [16–21] and oxides [22]. We have therefore undertaken the first systematic DFT level calculations, and associated IR spectral simulations, of CO over a family of related, isolated Pd clusters seeking to quantify the influence of particle size and CO coverage based only on the intrinsic properties of the metal NPs. The resulting calculations offer valuable insight into the fundamental processes that occur during CO adsorption over metal NPs under 'real world' conditions of high coverage and/or pressure [16].

CO adsorption on Pd surfaces and NPs has been investigated by both experiment and theory [4,23–26]. Early photoelectron diffraction experiments showed that at low coverage ($\theta = 0.1$–0.5) CO preferentially adsorbs at three-fold hollow sites on Pd(111) [27]. At higher coverage ($\theta = 0.6$–0.7) the preference switches to bridge sites, with atop species only appearing at very high surface densities ($\theta = 0.75$) [28]. Goodman and co-workers examined CO adsorption over Pd(111) and Pd(100) [29] single crystals at low and high coverage via temperature programmed desorption (TPD) and surface IR spectroscopy (RAIRS), uncovering a correlation between the activation energies for desorption and corresponding rates of CO oxidation. For Pd NPs, Wolter et al. performed a systematic study of CO over $Pd/Al_2O_3/NiAl(100)$. A strong atop signal was observed by RAIRS for small NPs (10–50 atoms), in addition to a contribution from bridge sites which becomes more important for larger particles. Upon heating, atop CO desorbed first leaving only bridge-bound molecules >335 K for 300 atom NPs. Dropsch and Baerns also studied CO adsorption on oxide supported Pd NPs by microcalorimetry and TPD [30], concluding that bridge-bound CO dominated at low coverages ($\theta < 0.4$), whereas three distinct CO species were observed at higher coverage. The size-dependence of CO adsorption on Pd NPs (120–4900 Pd atoms) supported over $Fe_3O_4/Pt(111)$ was also explored by single-crystal microcalorimetry [31,32]; a 20–40 kJ mol^{-1} decrease in adsorption energy was noted with CO coverage, similar to that predicted by DFT calculations for a Rh_4 nanocluster [16].

CO adsorption energetics have been extensively investigated by DFT over various transition and noble metal surfaces [33,34] and clusters [17,35]. In particular, it has been found that the site preference for CO adsorption on Pt(111) is incorrectly predicted by DFT methods, with predictions favouring high co-ordination CO adsorption sites over low co-ordination sites [34]. For Pd(111), three fold hollow sites are also calculated to provide the lowest adsorption energy for single CO molecules [36,37] although this is in agreement with STM, LEED [38] and SFG [25,39] studies. Rösch and coworkers recently calculated the size-dependent adsorption energy of CO on 13–116 atom Pd NPs [40,41] for various low coverage structures, identifying 50–100 atom clusters as the optimum to minimise CO adsorption, although this finding may have been influenced by the choice of the simple LDA functional, particularly in light of recent microcalorimetric data from Schauermann and co-workers which evidenced a decrease in adsorption energy with NP size [31].

Here we investigate the impact of Pd NP size and CO coverage on the energetics of CO adsorption, with a view to establishing a general framework within DFT for accurately simulating the IR vibrational spectra of CO over palladium nanoparticulate catalysts. Such a theoretical basis will aid the interpretation of experimental transmission and reflectance IR spectra in respect of the nature, number density, and adsorption strength of different CO species bound to practical catalysts, and hence enhance the utility of IR spectroscopies (transmission IR, DRIFTS, ATR-IR and RAIRS) routinely employed to determine the morphology and electronic structure of practical PGM catalysts [18,42]. We find that structural (e.g. average Pd—Pd and C—O bond lengths), energetic (e.g. CO adsorption enthalpy) and spectroscopic properties (e.g. C—O stretching frequency and band intensities) of the CO/Pd_n system evolve strongly with particle size and CO coverage. The coverage dependent heat of CO adsorption on Pd_{38} NP and associated relative stability of different adsorption sites are also rationalised.

2. Computational methods

Restricted and unrestricted DFT calculations were used, as implemented in Gaussian 09 [43], with the commonly used B3 exchange functional [44] combined with the LYP non-local correlation functional [45] (B3LYP). We also briefly tested other exchange–correlation (XC) functionals: M06-2X [46], TPSSh [47], LC-wPBE [48], PBE [49], and B3PW91 [44,50] (see supporting information, S-Fig. 1) which yielded the same relative total energy order for $Pd_4(3,1)$ at various spin multiplicities (s.m.). We adopted a computational strategy whereby the structures of $Pd_4(3,1)$ and $Pd_{13}(3,7,3)$ clusters were first fully optimised at a UB3LYP/CEP-121G(Pd), aug-cc-pVTZ(C,O) level of theory, in order to identify the possible adsorption configurations (e.g. linear, bridge and hollow). This level of theory was found sufficient among basis sets/ECP of varying size, LanL2mb [51,52], LanL2dz [52,53], CEP-121G [54,55], aug-cc-pVTZ [56–60] and QZVP [61,62], to yield converged adsorption energies (ΔE_{ads}) to within a few kJ mol^{-1} of the basis set superposition error (BSSE) corrected adsorption energies (ΔE_{BSSE}) obtained by the counterpoise method of Boys and Bernardi [63]. In Fig. 1 we show that the basis set/ECP CEP-121G(Pd),aug-cc-pVTZ(C,O) yields quantitatively similar results to the computationally intensive QZVP basis set that contains twice as many basis functions. Full optimization is critical [64] since strong adsorption-induced structural changes to the transition metal cluster were observed, especially for the Pd nanoclusters (i.e. $Pd_{4,13}$). Linear dependencies of the basis functions were removed by using the spherical version (5d and 7f) of these basis sets. The SCF convergence criteria for the root mean square (rms) density matrix and the total energy were respectively set to 10^{-8} e/$bohr^{-3}$ and 10^{-6} Hartree.

Calculations for the larger Pd_{38} NP were obtained via spin-polarised Γ point [65] calculations using VASP 5.3 [66,67]. Exchange and correlation effects were considered within the generalised gradient approximation (GGA) using the Perdew–Burke–Ernzerhof [68] (PBE) XC functional, with the projector augmented-wave (PAW) method [69,70] used to represent core states (1s for C and O, and 1s to 4p for Pd). The cut-off energy for plane-wave expansion was set to 500 eV. Nanoparticle/adsorbate models were centred within a 30 Å cubic box to ensure a sufficient vacuum gap around the cluster/adsorbate system. Geometry optimizations were performed with a residual force threshold of 0.015 eV $Å^{-1}$ using the conjugate-gradient algorithm. Convergence criteria for the electronic relaxation during optimization (frequency) calculations were based on the change of energy between

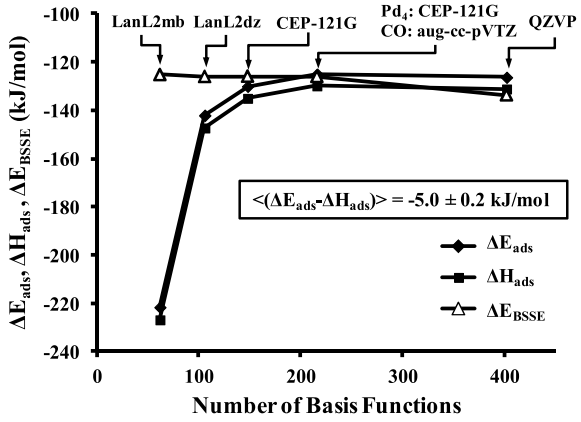

Fig. 1. Adsorption energy, enthalpy and BSSE-corrected adsorption energy as a function of the number of basis functions for Pd_4-lCO. Open shell calculations were also examined for spin contamination, which was found to be negligible.

SCF cycles with a threshold of 10^{-4} eV (10^{-7} eV). The initial charge density was obtained by superposition of atomic charges, and the projection operators were evaluated in reciprocal space.

We note that, for metallic systems, the B3LYP functional is not regularly used due to its failure to recover the homogeneous electron gas solution for itinerant electron states in bulk metals [71]. For metal complexes the functional is quite widely used and a combined B3LYP/CCSD(T) study has appeared for cationic group 10 and group 11 carbonyl complexes [72]. The nanoclusters considered here are intermediate in size. We use the B3LYP functional only for its reliability in vibrational analysis including intensity estimates for the IR modes of CO on the smaller clusters. The total adsorption energy per CO molecule ($\Delta E_{ads,CO}$) was calculated using Eq. 1,

$$\Delta E_{ads,\,CO} = \left(E_{Pdm(CO)n} - E_{Pdm} - n_{CO}.E_{CO}\right) / n_{CO} \quad (1)$$

where E_i is the total energy of fully optimised species i and n_{CO} is the number of adsorbed CO molecules. Note that this definition means that negative adsorption energies are favourable compared to gas phase CO and a free nanoparticle. The surface coverage of CO has been defined based on Eq. 2,

$$\theta_{CO} = n_{CO} / n_{Pd,surf} \quad (2)$$

where $n_{Pd,surf}$ is the number of surface Pd atoms of the NP. The vibrational frequencies were explicitly calculated by diagonalizing the Hessian matrix using the finite-difference (FD) method. Additional calculations using the density-functional-perturbation-theory (DFPT) method within VASP were used to ensure that agreement within 2 cm^{-1} could be obtained with this computational protocol. The relative intensities of linear-CO (lCO), bridge (bCO) and three-fold (3f) hollow (hCO) species were calibrated against the results for tetrahedral (T_d) Pd_4(3,1) and cubooctahedral (O_h) Pd_{13}(3,7,3). Infrared spectra were simulated by fitting a Lorentzian function with a FWHM = 15 cm^{-1}, centred at each stretching frequency calculated from the FD method.

3. Results and discussion

3.1. Effect of NP size on CO adsorption

Previous computational [41,64] and microcalorimetric [32] studies of CO adsorption on Pd NPs have suggested a strong cluster size-dependence of the adsorption energy. At low coverages, i.e. $\theta_{CO} < 0.1$ ML, CO adsorption energies can vary by almost 100 kJ mol^{-1} (falling from −202 kJ mol^{-1} for Pd_{13} to −109 kJ mol^{-1} for Pd_{25}), resulting in a critical cluster size (50–100 atoms) wherein CO adsorption is weakest [41]. Another microcalorimetry study showed that initial heats of adsorption that fall linearly with particle size from the Pd(111) surface value of 149 ± 3 kJ mol^{-1} down to 106 ± 1 kJ mol^{-1} for particles of 2 nm dimension [31]. Adsorption microcalorimetry offers precise adsorption heats [73,74], but no direct insight, into CO bonding modes. Atomistic simulations herein, provide adsorption energies of CO species according to their structural identification (i.e. lCO, bCO or hCO), however it is clear from the introductory discussion of site preference that this is likely to give insufficient accuracy to allow relative abundances (n_{lCO},n_{bCO},n_{hCO}) to be determined. However, DFT calculations can be used to interpret IR spectroscopic signatures of adsorbed CO species by obtaining the IR intensity factors as a function of CO position, and then using experimental data to interpret the site populations. IR intensity calculations are not currently available in VASP for these systems, and are most accurate using a hybrid functional method for which the computational expense increases rapidly with system size. Accordingly, we have performed calculations using small reference systems (Pd_4 and Pd_{13}), and extrapolated the results to the larger Pd_{38} cluster size. The choice of hybrid B3LYP functional for the calculation of IR oscillator frequencies was based on its earlier success in the spectral band assignment of diffuse reflectance infrared Fourier-Transform (DRIFT) spectra obtained for CO chemisorption over a highly dispersed Rh/γ-Al_2O_3 catalyst [18]. Due to computational cost, this method is limited to the smaller cluster sizes with single adsorbates. Therefore we additionally employed the more commonly used PBE functional for the largest cluster size, and to examine coverage effects.

Here, we briefly examine the dependence of CO adsorption energy on Pd cluster size, before considering the effect of CO surface coverage. The energetics of CO chemisorption were studied for three high symmetry Pd particles: tetrahedral Pd_4(3,1) (0.4 nm), cubooctahedral Pd_{13}(3,7,3) (0.8 nm) and cubooctahedral $Pd_{38}(O_h)$ (1.1 nm). Three distinct configurations were identified and are presented in Fig. 2: *linear* (lCO), *bridge* (bCO) and *hollow* (hCO) bound molecules, which resemble the stable adsorption configurations found over Rh_4(3,1) [10,17]. Additionally, di-carbonyl (di-CO) and tri-carbonyl species (tri-CO) were stable on Pd_4 but could not be identified on $Pd_{38}(O_h)$ and hence were not further considered; palladium dicarbonyl species are known to be particularly unstable [75], akin to their Rh analogues which are only found in supported catalysts as isolated mononuclear moieties [76,77]. Calculated adsorption energies of CO at a low coverage ($\theta \rightarrow 0$) are given in Table 1. For all adsorption sites we observe a strong particle size-dependence in good agreement with earlier theoretical studies [32,41,64]: on Pd_4 ΔE_{ads} = −130 to −257 kJ mol^{-1}; on Pd_{13} ΔE_{ads} = −167 to −223 kJ mol^{-1}; and for Pd_{38} ΔE_{ads} = −161 to −196 kJ mol^{-1}. Interestingly, this cluster size-dependence of CO adsorption energy was dependent on the adsorption configuration. For hollow and bridge-bound CO, $\Delta E_{ads,\,CO}$ indicates weaker binding with increasing NP size (0.4 nm → 1.1 nm), whereas linear bound CO becomes more strongly bound. The calculated sensitivity of CO adsorption energy to NP size scales roughly with the coordination number (i.e. number of Pd—C bonds), such that hCO > bCO > lCO.

According to these results, the experimentally observed trend should then depend on the site occupancies for the three positions which may be influenced by sample pre-treatment. Campbell and coworkers [31] suggested that the experimentally observed weakening of adsorption could result from a Van der Waals dispersion effect, which would be expected to reduce with particle size. We have used

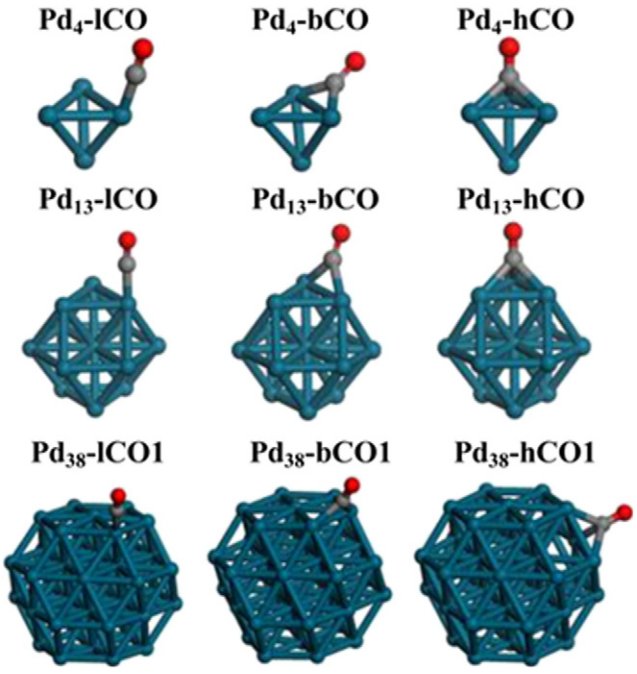

Fig. 2. Structures for linear, bridge and three-fold (3f) hollow bound CO on Pd_4(3,1), Pd_{13}(3,7,3) and $Pd_{38}(O_h)$, respectively.

Table 1
Vibrational stretching frequency, intensity, bond length and adsorption energy of CO(g), and CO on Pd_4 and Pd_{13} (B3LYP/CEP-121G(Pd),aug-cc-pVTZ(C,O)) and Pd_{38} (PBE, planewaves, E_{cut} = 500 eV, 30 Å cubic box), NPs respectively. The optimised structures of Pd_4, Pd_{13} and Pd_{38} had a s.m. of 3, 7 and 9, respectively (S-Fig. 1).

Label	p.g.[a]	s.m.[b]	ν^b_{C-O} (cm^{-1})	I^b_{C-O} (10^6 m mol^{-1})	r^b_{C-O} (Å)	ΔE_{ads} (kJ mol^{-1})
Pd_4-lCO	C_1	3	2102	1125	1.139	−130
Pd_4-bCO	C_{2v}	1	1879	587	1.171	−208
Pd_4-hCO	C_{3v}	1	1768	475	1.187	−257
Pd_{13}-lCO	C_s	3	2088	1396	1.142	−149
Pd_{13}-bCO	C_s	3	1931	955	1.161	−198
Pd_{13}-hCO	C_{3v}	3	1827	815	1.175	−200
Pd_{38}-lCO1	C_s	9[c]	2058	–	1.150	−161
Pd_{38}-bCO1	C_s	9[c]	1886	–	1.171	−189
Pd_{38}-hCO1	C_s	9[c]	1786	–	1.185	−196
CO(g)	$D_{\infty h}$	1	2131	–	1.133	–

[a] p. g. = point group symmetry.
[b] s.m. = spin multiplicity = 2S + 1.
[c] Spin-polarised calculation.

the PBE-D2 method to test if dispersion energy is a significant factor and the results are presented in Table S1. The dispersion contribution to adsorption energies was small, and does not affect the observed trend with cluster size. The D2 correction is an atom–atom interaction model which does not include dispersion interactions with the delocalised electrons of a metal. Nevertheless, these calculations indicate that dispersion effects for CO on metals at low coverage are likely negligible. We speculate that the trend in adsorption energy with particle size reported by Campbell may be an indication that the hollow and bridge site populations were high in their experiments.

In Table 1, the stretching frequency (ν_{C-O}), IR intensity (I_{C-O}), bondlength (r_{C-O}) are also presented for the various configurations. Data for Pd_4 and Pd_{13} are at the B3LYP level with a localised basis set so that calculated IR intensities can be included. We note that a linear adsorption mode results in a larger transition dipole moment than either hollow or bridge sites. For the Pd_4 cluster, a singlet state was energetically favourable for the bridge and hollow adsorption modes, but for Pd_4-lCO and the bare Pd_4 cluster the triplet state is lower in energy, in agreement with an earlier study using B3LYP/LanL2dz [78] and detailed MCSCF studies of the low lying states of Pd_4 [79]. For Pd_{13}, we find the triplet state to be the lowest lying for all geometries, and for Pd_{38} a s.m. of 9 is found. This is consistent with the increased number and decreased energetic spacing of the metal electronic states as the cluster size is increased.

A linear correlation between CO bondlength and vibrational frequency was observed for all cluster sizes (Fig. 3a). For any adsorbed state, r_{C-O} was longer and the stretching frequency lower than in the gas phase, evidencing adsorption-induced weakening of the CO bond in accordance with the Blyholder model [80]. This trend also seems insensitive to the choice of functional, since B3LYP and PBE data follow the same trendline. Similar correlations have been reported for Rh_4(3,1) clusters using smaller atom-centred basis sets (i.e. LanL2dz) [18], and a similar decrease in ν_{lCO} observed via Infrared multiple photon dissociation (IR-MPD) spectroscopy for neutral Pd_nCO clusters where n = 6, 7, 8 and 9 [81]. It is evident from Fig. 3b that the CO bond weakens (ν_{C-O}) as the metal–carbonyl bond strength (ΔE_{ads}), increases, again consistent with the Blyholder model. The IR intensities of various adsorbed configurations roughly scaled in the same fashion for lCO, bCO and hCO species on Pd_4(3,1) and $Pd_{13}(O_h)$, with lCO:bCO:hCO = 1.00:0.68:0.58 (Fig. 4). This intensity ratio was therefore employed to estimate relative band intensities during the IR simulations described later. In summary, the vibrational frequencies (ν_{C-O}) and intensities (I_{C-O}) of adsorbed CO are inversely proportional to the exothermicity of adsorption.

To the best of our knowledge, experimental singleton CO frequencies have never been measured for supported Pd nanoparticles under

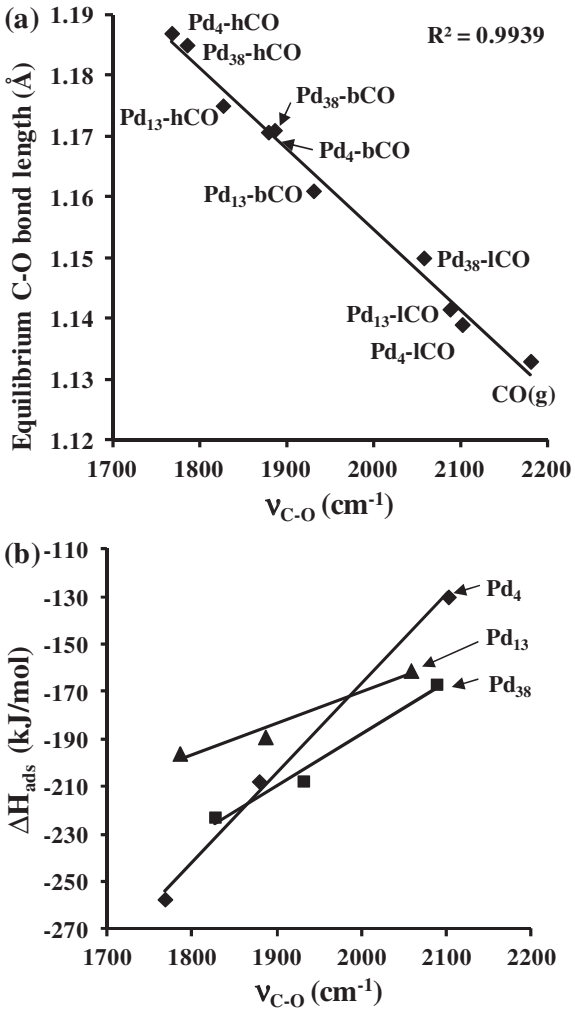

Fig. 3. Correlation between (a) equilibrium C—O bondlength and CO vibrational frequency, and (b) CO adsorption energy and CO vibrational frequency, for a CO molecule on Pd_4, Pd_{13} (B3LYP/CEP-121G(Pd),aug-cc-pVTZ(C,O)) and Pd_{38} (PBE, planewaves, E_{cut} = 500 eV, 30 Å cubic box) NPs.

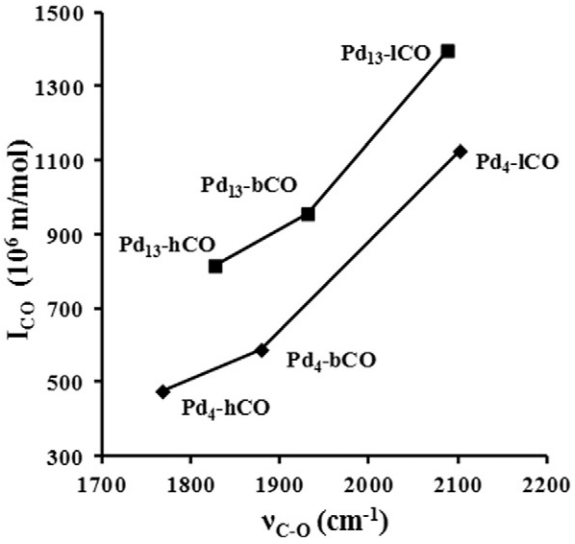

Fig. 4. Correlation between the IR absorption intensity and CO vibrational frequency (B3LYP/CEP-121G(Pd),aug-cc-pVTZ(C,O)) for a CO molecule on Pd_4 and Pd_{13} NPs.

conditions wherein adsorption of only a single CO molecule per nanoparticle has been proven unequivocally. Freund and co-workers investigated CO adsorption over 3.5 nm Pd nanoparticles supported on alumina by SFG at pressures between 10^{-7} and 200 mbar CO [24], observing multiple site occupancy for the smaller particles at room temperature, even under the lowest pressures, albeit with a linearly adsorbed CO frequency of 2082 cm^{-1}, in good agreement with our calculations for Pd_4-lCO, Pd_{13}-lCO and Pd_{39}-lCO in Table 1, which span 2058–2102 cm^{-1}. Similar multiple adsorption site occupancy was also observed for Pd clusters deposited over ultrathin silica films on Mo(110) at 10^{-8} Torr CO [82], although frequencies for linear and bridge/hollow adsorbed CO of 2068 and 1920 cm^{-1} respectively are likewise in agreement with Table 2. Hence our computed singleton CO frequencies for linearly and bridge bound CO are close to experimental values reported for Pd nanoparticles under conditions most likely to favour singleton adsorption. There have been few attempts to experimentally determine the absorption intensities of CO occupying different adsorption sites over Pd nanoparticles, although Vannice and Wang report extinction coefficients for Al_2O_3, SiO_2, TiO_2 and SiO_2–Al_2O_3 supported Pd particles via transmission IR measurements [83]. Their experimental study estimated that extinction coefficients for bridge-bound CO were significantly larger than those than linearly adsorbed CO (4.1×10^6 versus 0.36×10^6 cm^2 mol^{-1}). This contrasts with our preceding calculations for singleton CO adsorption, which suggest that linear adsorption modes are approximately 50% more intense than bridging mode, however the experimental values were determined for saturation CO coverages over Pd nanoparticles of undefined size, in which lateral interactions between CO molecules cannot be discounted, nor adsorption site assignments unequivocally proven. These experimentally-determined extinction coefficients also exhibited a wide (between 4- and 10-fold) variation for linear and bridge bound CO over Pd across the different oxide supports, and hence there remains a need for further experimental studies of CO adsorption over size-controlled Pd nanoparticles under low (single molecule) coverages.

3.2. Low coverage CO adsorption on Pd_{38}

In order to further explore the adsorption energetics of CO as $\theta_{CO} \rightarrow 0$, additional calculations were undertaken for CO placed at every symmetry unique linear, bridge and hollow position on the cubooctahedral Pd_{38} NP (Fig. 5), using the PBE functional. Full optimisation of the NP/adsorbate system showed that certain adsorbed configurations were unstable (e.g. bCO2, bCO4), with the CO molecule relaxing into adjacent adsorption sites.

Table 2
Adsorption energy per CO on a Pd_{38} NP as a function of CO coverage and adsorption site.

Label[a]	Formula	θ_{CO}[b]	$\Delta E_{ads,CO}$[c]	n_{hCO}	n_{bCO}	n_{lCO}
$32COh_{10}b_{22}l_0$	$Pd_{38}(CO)_{32}$	1.000	−160	10	22	0
$20COh_{16}b_4l_0$	$Pd_{38}(CO)_{20}$	0.625	−180	16	4	0
$16COh_{16}b_0l_0$	$Pd_{38}(CO)_{16}$	0.500	−184	16	0	0
$12COh_{12}b_0l_0$	$Pd_{38}(CO)_{12}$	0.375	−186	12	0	0
$8COh_8b_0l_0$	$Pd_{38}(CO)_8$	0.250	−191	8	0	0
$4COh_4b_0l_0$	$Pd_{38}(CO)_4$	0.125	−202	4	0	0
$2COh_2b_0l_0$	$Pd_{38}(CO)_2$	0.063	−199	2	0	0
$COh_1b_0l_0$	$Pd_{38}(CO)_1$	0.031	−204	1	0	0
$32COh_{10}b_7l_{15}$	$Pd_{38}(CO)_{32}$	1.000	−158	10	7	15
$24COh_2b_9l_{13}$	$Pd_{38}(CO)_{24}$	0.750	−165	2	9	13
$12COh_0b_0l_{12}$	$Pd_{38}(CO)_{12}$	0.375	−165	0	0	12
$6COh_0b_0l_6$	$Pd_{38}(CO)_6$	0.188	−164	0	0	6
$4COh_0b_0l_4$	$Pd_{38}(CO)_4$	0.125	−165	0	0	4
$2COh_0b_0l_2$	$Pd_{38}(CO)_2$	0.063	−165	0	0	2
lCO1	$Pd_{38}(CO)_1$	0.031	−161	0	0	1
	Pd_{38}	0.000	–	–	–	–

[a] Entries 2–8 and 9–15 have been calculated via algorithm 1 and 2, respectively.
[b] CO surface coverage given by n_{CO}/n_{surf}, where $n_{surf} = 32$ for Pd_{38}.
[c] Adsorption energy change per CO in kJ/mol calculated using Eqn. 1.

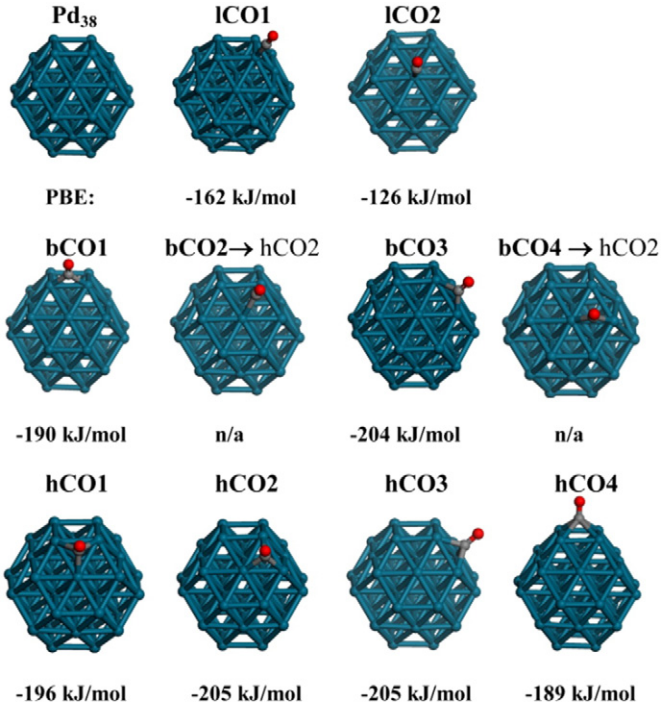

Fig. 5. Symmetry unique adsorption sites and energies for $Pd_{38}CO$ using the PBE XC functional.

As expected, for the PBE functional, we find that linearly adsorbed CO has a lower adsorption energy on Pd_{38} than bridge/hollow-bound CO. The weakest bound CO species on Pd_{38} corresponded to linearly adsorbed CO at the vertex of the (100)-facet (lCO1 = $lCO_{(100)}$), followed by linearly adsorbed CO on a (111)-facet (lCO2 = $lCO_{(111)}$), with four-fold hollow-bound CO at the (100)-site (hCO4 = $hCO_{(100)}$) exhibiting a moderate adsorption strength. Bridge- (bCO1 = $bCO_{(100/111)}$) and hollow-bound CO (hCO1 = $hCO_{(100/111)}$) at the edge of the (100)/(111) facet were the next most stable configurations. The strongest adsorption site for CO at $\theta_{CO} \rightarrow 0$ was the 3f hollow bound CO (i.e. hCO2, hCO3 = $hCO_{(111/111)}$) to the (111)-like facets, or at the bridge site between two (111)-facets (bCO3 = $bCO_{(111/111)}$). Bridge-bound CO between two (111)-facets has been previously described as the most stable adsorption configuration for CO on alumina-supported Pd NPs [23]. Our calculations suggest that the 3f hollow bound CO (i.e. $hCO_{(111)}$) is practically isoenergetic with this for $\theta_{CO} \rightarrow 0$, in keeping with the previously reported weak facet specificity for CO adsorption in the low coverage limit [31]. In the following section we briefly evaluate the interaction of two hCO molecules on the Pd_{38} surface before considering adsorption energetics at higher CO coverages.

3.3. High coverage CO adsorption on Pd_{38}

The influence of lateral interactions and charge sharing upon CO binding to a Pd_{38} NP was studied by progressively increasing the number of co-adsorbed molecules. Structures in which two CO molecules were co-adsorbed at 3f hollow sites on Pd_{38} were probed first, and a selection of these configurations is presented in Fig. 6. The most favourable scenario for this system is that in which both CO molecules share one Pd atom (i.e. 2hCO1), however sharing of a second Pd atom (e.g. 2hCO2) destabilised adsorption by ~18 kJ mol^{-1}. The absence of any shared Pd atoms (e.g. 2hCO3) is likewise disfavoured (by 11 kJ mol^{-1}) compared to that wherein a single surface Pd atom is shared.

A similar phenomenon is observed for four co-adsorbed CO molecules, for which the most stable structures are those in which all CO

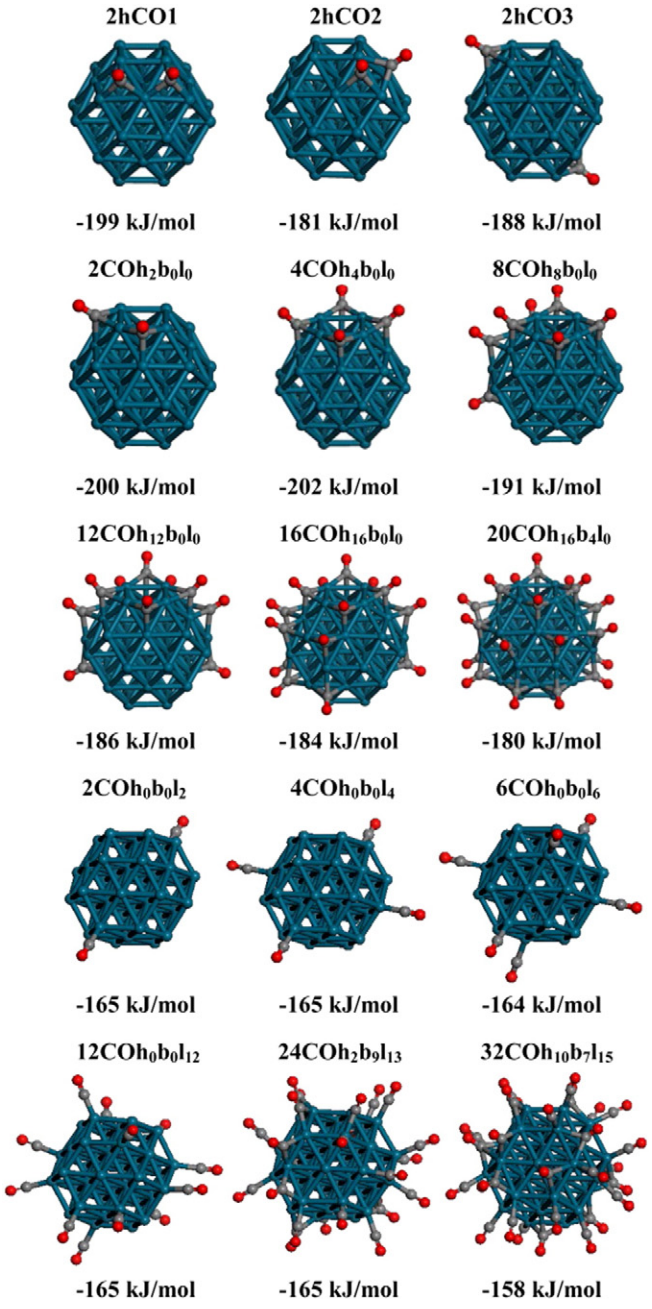

Fig. 6. Structures and PBE adsorption energies per CO molecule of fully relaxed $Pd_{38}(CO)_n$, where n = 2, 4, 6, 8, 12, 16, 20, 24, 32. Initial geometries obtained with coverage *algorithms 1* and *2*.

molecules share a single Pd atom, resulting in a ring of CO molecules around the (100) facet ($4COh_4b_0l_0$ in Fig. 6). The diffusion barrier of CO on Pd(110) surfaces determined by inelastic tunneling microscopy is 17.4 kJ mol^{-1} [84]. At high coverages, this barrier is expected to fall, according to time-elapsed STM diffusivity studies of CO on Cu(111) which showed a doubling in the hopping rate with increasing local CO coverage [85]. Based on our static results above, and assuming fast CO diffusion kinetics on the NP surface, one would expect that all 3f hollow sites surrounding the six 4f hollow sites of Pd_{38} would be occupied first as the CO coverage is further increased. We used this concept to create one set of models for predominantly hollow-bound $Pd_{38}(CO)_n$ through *algorithm 1*. Specifically, algorithm 1 involves: (a) occupy all 3f hollow sites around one of the six 4f hollows; then (b) add CO molecules to 3f hollow positions around adjacent 4f hollows while maximising the number of single, shared, Pd atoms between any two adsorbates; and finally (c) perform a full optimisation without symmetry constraints to permit relaxation to other bound configurations. The resulting structures built implementing *algorithm 1* are presented in Fig. 6 ($20COh_{16}b_4l_0$, $16COh_{16}b_0l_0$, $12COh_{12}b_0l_0$, $8COh_8b_0l_0$, and $4COh_4b_0l_0$), their associated energetics plotted against cluster size in Fig. 7, and more detailed data provided in Table 2. This methodology suggested that, even at the highest coverages, only hollow and bridge sites were occupied in the optimised structures. Using just *algorithm 1*, linearly-bound CO would not be sampled, and hence a second approach was also used to produce alternative site occupancies.

The second algorithm adopts a different approach based around the 'domino effect', to model repulsive interactions between high coverages of adjacent, linearly adsorbed CO molecules, rationalised previously for a Rh_4(3,1) cluster [16] and to simulate low coverage adsorption from a less dense gas phase. *Algorithm 2* proceeds as follows: (a) place CO molecules on atop positions with their molecular axes pointing towards the centre of mass of the NP; then (b) adjust bondlengths so that all Pd—C and C—O bonds lengths equal 2.050 and 1.115 Å respectively, to emulate chemisorption from a weakly bound state; and finally (c) perform a full optimisation without symmetry constraints to permit relaxation of linear CO to bridge and hollow sites. This algorithm was utilised to generate the structures $32COh_{10}b_7l_{15}$, $24COh_2b_9l_{13}$, $12COh_0b_0l_{12}$, $6COh_0b_0l_6$, $4COh_0b_0l_4$, $2COh_0b_0l_2$ and $COh_0b_0l_1$, which are also included in Fig. 6 and Fig. 7 with additional detail in Table 2.

Algorithm 1 was based on observations from low PBE-energy arrangements for two and four CO molecules, wherein all possible adsorption combinations could be easily tested. *Algorithm 2* affords an additional test that initially places all CO molecules in the least energetically favourable atop site, such that at low coverages, adsorbate–adsorbate repulsive interactions are weak and CO molecules are trapped in local minima that prevent their relaxation into lower energy bridge and hollow sites; at high coverages, strong repulsive interactions enable linearly-bound CO to overcome small barriers associated with their movement into bridge or hollow sites, producing configurations in which all three types of adsorption site are populated. Such local energy minima in the DFT calculations are more likely to correspond to the experimental situation, wherein an atop preference should be observed at low coverage [86].

Fig. 7 shows that at low coverages *algorithm 2* yields much less favourable DFT adsorption energies than *algorithm 1*, since the former preserves as many as 12 linearly-bound CO molecules, whereas only hollow sites are occupied post-relaxation via the latter approach (see Table 2). We note that the adsorption energy per CO molecule weakens with increasing θ_{CO} for *algorithm 1*, but remains constant for *algorithm 2*. The coverage-dependent adsorption energy predicted by *algorithm 1* is

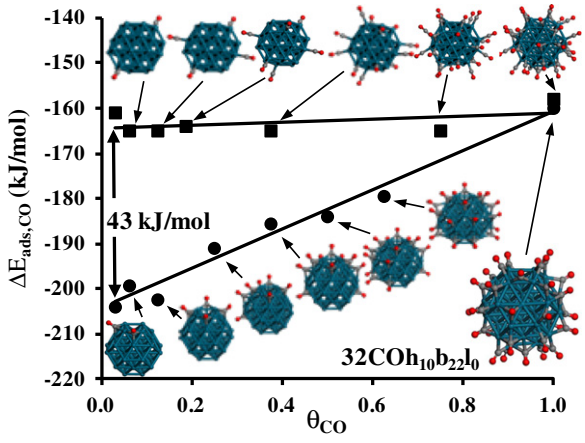

Fig. 7. Coverage dependent CO adsorption energy ($\Delta E_{ads,CO}$, PBE) per molecule over cubooctahedral Pd_{38} for structures obtained via (•) *algorithm 1* and (■) *algorithm 2*, and for $32COh_{10}b_{22}l_0$. Solid lines are least square fits to data points.

in good agreement with microcalorimetric measurements of CO on supported model Pd NPs [31,32,87], which show a 20–40 kJ mol^{-1} decrease with θ_{CO}, and previous calculations on a Rh nanocluster which showed a 60 kJ mol^{-1} fall in the heat of CO adsorption with coverage [16]. Microcalorimetric measurements of the heats of CO adsorption on Pd/Al_2O_3, SiO_2 and TiO_2 having loadings of 2, 5 and 10 wt% Pd reported values spanning 99–162 kJ mol^{-1} [30], with high adsorption energies associated with low Pd loadings (i.e. smaller) and highly reduced particles. Our calculated, average CO adsorption energy of -159 ± 1 kJ mol^{-1} on Pd_{38} for $\theta = 1$ is in good agreement with the -162 kJ mol^{-1} measured by Dropsch and Baerns [30]. We have also explored two higher coverage regimes, $Pd_{38}(CO)_{38}$ ($\theta = 1.50$) and $Pd_{38}(CO)_{54}$ ($\theta = 1.69$), which yielded even lower heats of adsorption of -123.0 kJ mol^{-1} and -112.4 kJ mol^{-1} respectively.

It is interesting to note that (at low coverages) CO bound in hollow sites is up to 43 kJ mol^{-1} more stable than that adsorbed in linear sites. However, this large energetic difference between linear and hollow bound CO vanishes at higher coverages (e.g. $20COh_{16}b_4l_0$ and $24COh_2b_9l_{13}$). We have further tested this convergence by optimising a saturated CO monolayer structure ($32COh_{10}b_7l_{15}$, see Table 3). For this limiting coverage regime, the energy difference per CO molecule for different configurations (e.g. $32COh_{10}b_{22}l_0$ versus $32COh_{10}b_7l_{15}$) falls below the threshold of thermal diffusion at STP (<2.5 kJ mol^{-1}), suggesting that adsorption site populations will be fluxional as CO coverage nears saturation. Explicit calculation of the diffusion barrier at $\theta = 1$ was not possible due to the *coupled diffusion of CO* molecules on Pd NP at high coverages. For example, for $32COh_{12}b_7l_{13}$, the movement of one of the linearly-bound CO ($lC_{23}O_{10}$, see ESI for atom labels) to a nearby hollow-bound position causes the simultaneous relaxation of hC_7O_{14} to bCO and $lC_{30}O_{31}$ to bCO. In another case ($32CO'h_{12}b_7l_{13}$), movement of $bC_{22}O_{28}$ to a hollow site causes the simultaneous relaxation of lC_6O_{13} and $lC_{18}O_7$ to hollows, and $lCO_{13}O_3$ to a bridge site. In all cases examined, displacement of a single CO molecule triggered site-switching of multiple other co-adsorbates; the CO molecules so perturbed were not necessarily neighbouring the initially displaced CO molecule, but on occasion on the opposite side of the NP. Table 3 shows that the structures resulting from these displacements have close relative energies despite significant differences in their site populations. Experimental IR spectra of CO over Pd nanoparticles are measured almost exclusively at 'high' pressure/saturation θ_{CO} [15,23,88–90], hence it seems plausible that *algorithm 2*, which incorporates repulsive interactions between co-adsorbates and generates linear, bridge and hollow CO species, may be the most apposite among the 2 algorithms for simulating IR spectra of such Pd NP systems. Indeed, we later show that simulated IR absorption spectra using *algorithm 2* are in good agreement with experimental data for silica supported palladium NPs.

Dropsch and Baerns also obtained coverage-dependent TPD-CO spectra that show a shift to lower temperature as a function of CO coverage, consistent with the falling heats of CO adsorption observe in Fig. 7 [30]. At coverages <0.4 ML they only observed one CO desorption peak, while higher coverages resulted in three distinct adsorption states, consistent with the computed thermodynamic stability of hollow-bound CO at low coverage, and population of three bonding sites at $\theta_{CO} = 1$ as noted above. This TPD study also concluded that bridge-bound CO was the most abundant form over Pd NPs. From a thermodynamic viewpoint our calculations yield a similar conclusion, with the lowest energy structure for $Pd_{38}(CO)_{32}$ comprising mostly bridge-bound CO (i.e. $32COh_{10}b_{22}l_0$), and a minority hollow-bound. High CO coverages appear to energetically favour chains of bridged molecules, which may be closed, or as in this work, terminated by linear carbon monoxide (Scheme 1). Such chains of bridging CO molecules decorate the edges of the $Pd_{38}(O_h)$ cubooctahedron, in line with high pressure (200 mbar) SFG studies which showed the existence of such CO species under catalytically relevant reaction conditions [23].

It is conceivable that the motion in such CO chains is coupled, and indeed our subsequent vibrational analysis suggests that frequency-splitting occurs, demonstrating vibrational coupling of CO stretches; such as splitting/shifting of CO vibrational bands has been previously reported on surfaces [91] and metal NPs [18]. Other thermodynamically stable structural motifs were also identified. For example, lCO-hCO-lCO and even lCO-hCO-lCO-hCO-lCO appeared in the optimised structures to have greater thermodynamic stability than isolated adsorbed CO configurations which one may have expected on the basis of reducing repulsive inter-adsorbate interactions.

3.4. IR simulations of $Pd_{38}(CO)_n$

At the PBE level, using a 30 Å cubic periodic box, the calculated vibrational frequency of gas phase CO is $\nu_{CO,PBE} = 2131$ cm^{-1} which is 49 cm^{-1} below the experimental value ($\nu_{exp} = 2180$ cm^{-1}) from earlier DRIFTS measurements [18]. Note that the spectral resolution of most experimental studies precludes discrimination of R and P branches and hence accurate reporting of frequencies relative to the vibrational band centre.We therefore add 49 cm^{-1} to the calculated vibrational frequencies for the PBE simulations using CO on the Pd_{38} cluster to simplify comparison with experimental data. IR simulations based on these intensity estimates from B3LYP calculations of the smaller clusters where carried out using optimised structures from *algorithm 1* ($20COh_{16}b_4l_0$, $16COh_{16}b_0l_0$, $12COh_{12}b_0l_0$, $8COh_8b_0l_0$, $4COh_4b_0l_0$) and *algorithm 2* ($32COh_{10}b_7l_{15}$, $24COh_2b_9l_{13}$, $12COh_0b_0l_{12}$, $6COh_0b_0l_6$, $4COh_0b_0l_4$, $2COh_0b_0l_2$, $COh_0b_0l_1$). Simulated spectra are shown in

Table 3
Relative average CO adsorption energy as a function of adsorption site population at $\theta_{CO} = 1$.

Label	$r\Delta E_{ads}$[a]	n_{hCO}	n_{bCO}	n_{lCO}	Action
$32COh_{10}b_7l_{15}$	0.0	10	7	15	Original
$32COh_{12}b_7l_{13}$	0.1	12	7	13	lCO to hCO
$32CO'h_{12}b_7l_{13}$	−1.0	12	7	13	bCO to hCO
$32COh_{11}b_9l_{12}$	−1.9	11	9	12	lCO to bCO
$32COh_{10}b_{22}l_0$	−2.3	10	22	0	All lCO to bCO

[a] Relative ΔE is difference between the ΔE per CO of 32lCO to that of $Pd_{38}(CO)_{32}$ where the number of each CO species was altered.

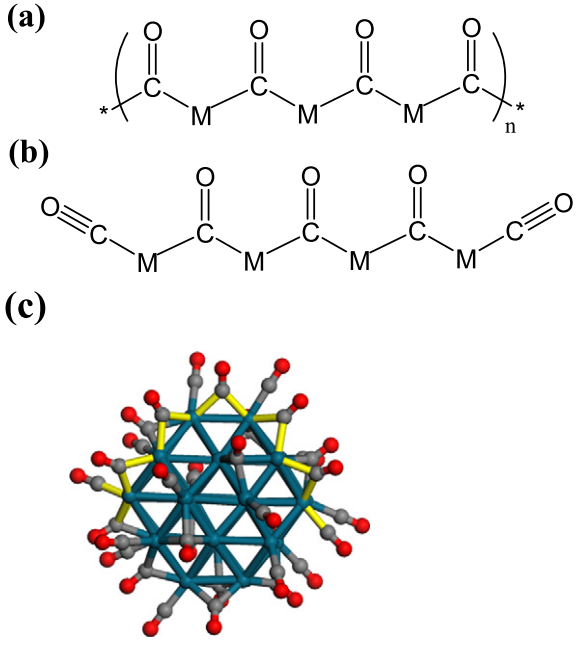

Scheme 1. Schematic of (a) closed and (b) open bridge-bound CO chains on a Pd_{38} NP, and (c) three-dimensional ball and stick representation of $Pd_{38}(CO)_{32}$ showing open bridge CO chain in yellow.

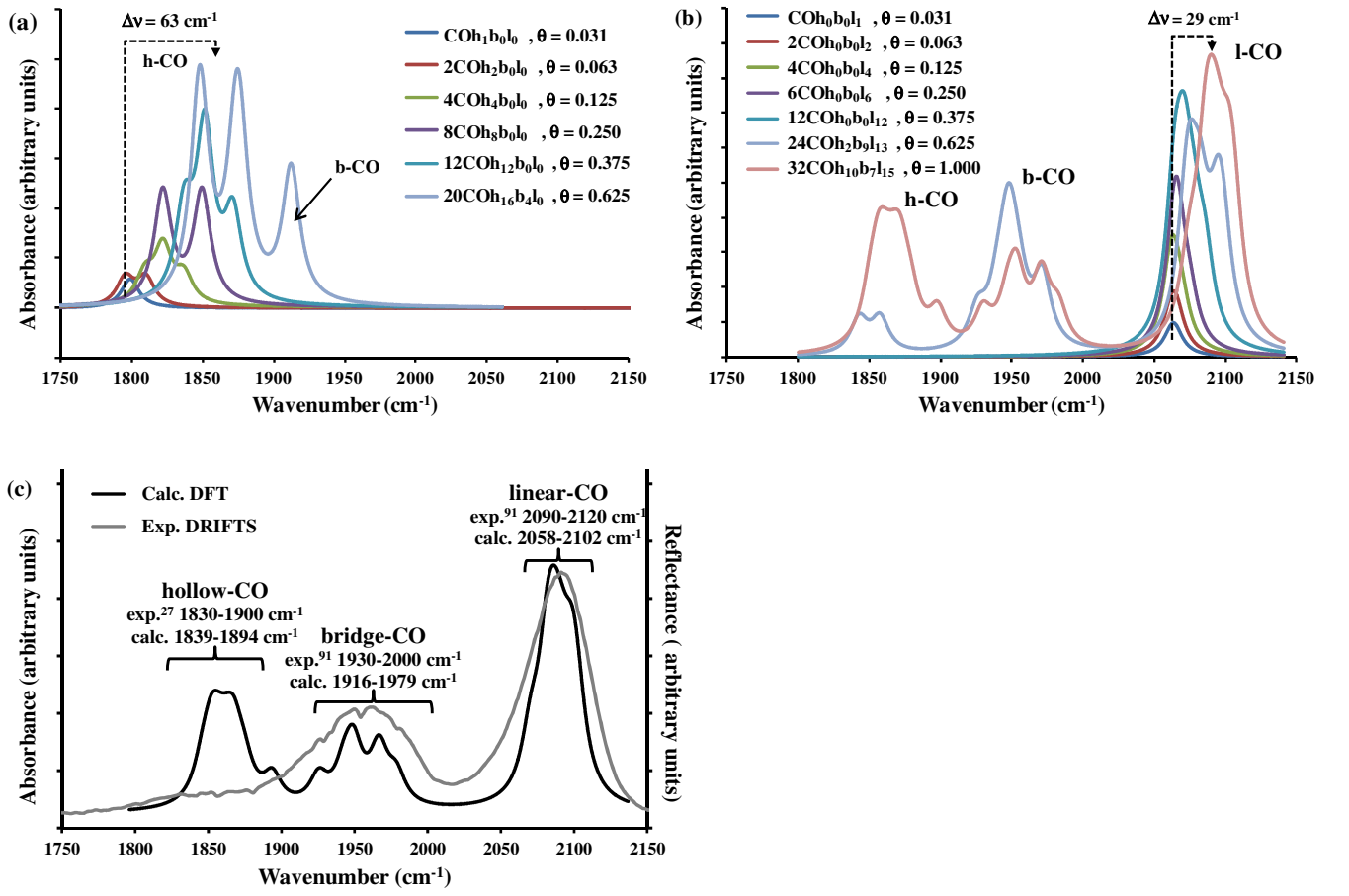

Fig. 8. Simulated IR absorption spectra for a range of $Pd_{38}(CO)_n$ structures created with (a) *algorithm 1*, (b) *algorithm 2* and (c) comparison of *algorithm 2* with experimental DRIFTS spectrum of CO on Pd/KIT-6 for $\theta_{CO} = 1$. Oscillator intensities scaled in the ratio lCO:bCO:hCO = 1.00:0.68:0.58 taken from Pd_{13} in Fig. 4. Frequencies have been shifted by 49 cm^{-1} which is the difference between the calculated vibrational frequency of gas phase CO ($\nu_{CO,PBE} = 2131\ cm^{-1}$) and the experimental value ($\nu_{exp} = 2180\ cm^{-1}$) [18].

Fig. 8a–b, alongside a comparative experimental DRIFTS spectrum for CO adsorbed over a 2.22 wt% Pd/KIT-6 mesoporous catalyst, with mean Pd NP diameter of 1.7 nm (Fig. 8c).

IR spectra simulated via *algorithm 1* display significant vibrational coupling, evidenced by fine structure within the hollow-bound CO band, which (albeit infrequently present) appears as a weak, broad feature in DRIFT spectra of supported catalysts [18]. Fig. 8a also shows the presence of bridge-bound CO at intermediate coverages ($\theta_{CO} = 0.625$), which overlaps with hollow CO features, indicative of similar adsorption energetics at high coverage. The latter observation is consistent with the weakening Pd—hCO bond with increasing θ_{CO} from 0.03 → 0.625 apparent in Fig. 7, which induces a pronounced 63 cm^{-1} blue-shift in the hCO band average position. A similar, albeit, weaker blue-shift (29 cm^{-1}, Fig. 8b) was observed with increasing θ_{CO} for linearly-bound CO bands simulated via *algorithm 2*.

The utility of these simulations was assessed for $Pd_{38}(CO)_{32}$ by benchmarking against frequency ranges and band assignment for RAIRS studies on model Pd/Al_2O_3 catalysts [86] and vibrational sum frequency generation (SFG) of CO adsorption on Pd NPs and Pd(111) surfaces [39]. The RAIRS study of Wolter et al. recorded absorption spectra for CO on nanoparticles ranging from $Pd_{<10}$ to Pd_{7100} at 90 and 300 K. Features between 1930 and 2000 cm^{-1} were assigned to bridge-bound CO, and those between 2090 and 2120 cm^{-1} to linearly-bound CO. These compare extremely favourably to corresponding predictions of 1920–1983 cm^{-1} and 2062–2106 cm^{-1} from our simulations using *algorithm 2* (Fig. 8b). The signal from hollow CO (hCO) was reported to be weak in these RAIRS experiments, however photoelectron diffraction studies [27] and RAIRS measurements over Pd(111) at temperatures <200 K and >350 K [92] suggest an indicative stretching frequency between 1825 and 1900 cm^{-1} (cf. 1843 and 1898 cm^{-1} in Fig. 8c). Agreement between the present calculations at $\theta_{CO} = 1$ via *algorithm 2* and experimental observations is astonishingly good. Band positions and relative intensities of linear and bridge-bound CO from our simulations are also in excellent correspondence with the DRIFT spectrum of a saturated CO adlayer over a 2.22 wt% Pd/KIT-6 catalyst [15] (Fig. 8c). The extremely weak experimental hCO band for Pd NPs supported on the KIT-6 mesoporous silica likely reflects a combination of (i) the smaller IR absorption coefficients with respect to bCO and lCO (Fig. 4), and (ii) the experimental protocol, in which the Pd catalyst was flushed with an inert gas after CO adsorption at 298 K prior to spectral acquisition [15]; thermodynamics suggest that CO is only stable in hollow sites at ambient temperature under CO partial pressures exceeding 1000 mbar [92].

3.5. Coverage-dependent blue-shift of CO on Pd_{38}

The preceding coverage-dependent vibrational frequencies for CO in each of the three adsorption sites over a $Pd_{38}(O_h)$ NP derived via *algorithms 1* and *2* are summarised in Fig. 9. In all cases, the CO stretch exhibited a significant blue-shift with increasing coverage, with the sensitivity of this shift in the order hCO > bCO > lCO, akin to that observed in electrochemical RAIRS studies of CO adlayers on Pd(110), which demonstrated a 10 cm^{-1} blue-shift for $\theta_{CO} = 0 \rightarrow 1$ [93]. We attribute the stronger coverage-dependence observed herein to quantum size effects, and note that an earlier study of CO adsorption on $Rh_4(3,1)$ reported an even greater blue-shift of 80 cm^{-1} [16]. The coverage-dependent blue-shift may therefore provide a means by which to differentiate between hollow and bridge/linear bound CO in experimental IR

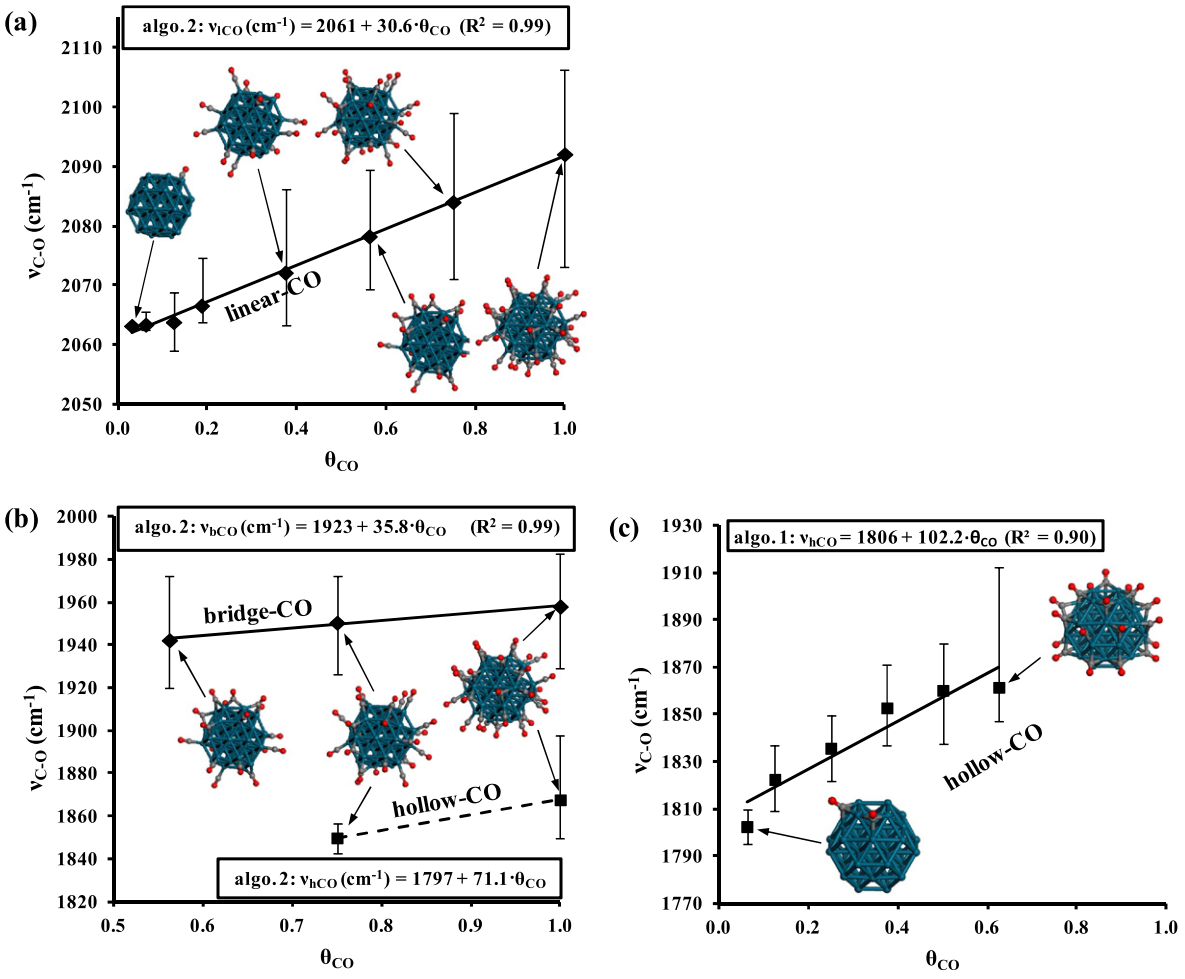

Fig. 9. Mean CO vibrational stretching frequency of (a) linear and (b) bridge (—) and hollow (—) bound CO from *algorithm 2*, and (c) hollow bound CO from *algorithm 1*, as a function of θ_{CO} on a Pd_{38} NP. Error bars show the maximum/minimum values.

spectroscopy. This consistent blue-shift for all adsorption configurations indicates strengthening of the C—O bond, and concurrent weakening of the M-CO bond. Based on the Blyholder [80] and Bagus [94] interpretations of the metal–carbonyl bond, this weakening reflects reduced electron donation from occupied d-states on the metal into the doubly degenerate, anti-bonding $2\pi^*$ molecular orbital of CO, increasing the covalency of the C═O bond and hence force constant.

3.6. Coverage-dependent isotropic expansion of Pd_{38}

Adsorbate-induced lattice expansion is well known for extended surfaces and NPs through diffraction studies [95], and has been demonstrated computationally for hydrogen on Pd_6 and Pd_{13} NPs [96]. In view of the above variation in CO adsorption strength with coverage, we therefore computed the mean Pd—Pd bondlength ($r_{<Pd-Pd>}$) and accompanying variance ($\sigma_{<Pd-Pd>}$) in order to identify whether a similar lattice expansion occurs in the $Pd_{38}(CO)_n$ system. Results of this analysis are shown in Fig. 10 for structures obtained via *algorithms 1* and *2*. The average Pd—Pd bondlength of the Pd_{38} NP increased by >3.5% as $\theta_{CO} = 0 \rightarrow 1$, a striking lattice expansion that was approximately proportional to the number of adsorbed CO molecules. The origin of this expansion lies in the overall increase in charge transfer from the Pd_{38} NP into adsorbate bonds with increasing CO coverage, and hence weaker cohesive metallic bonding. It is important to note that while the adsorption energy per CO molecule falls with θ_{CO} from approximately -200 kJ mol^{-1} over the bare particle to -160 kJ mol^{-1} at saturation, this is more than compensated for by the increasing number of Pd—CO bonds formed, and hence rise in total adsorption energy and consequent perturbation of the intraparticle bonding. Structures derived by *algorithm 1* always exhibited larger expansions than those derived by *algorithm 2*, although the associated spread of bondlengths $\sigma_{<Pd-Pd>}$ was also greater. Both these observations are consistent with stronger

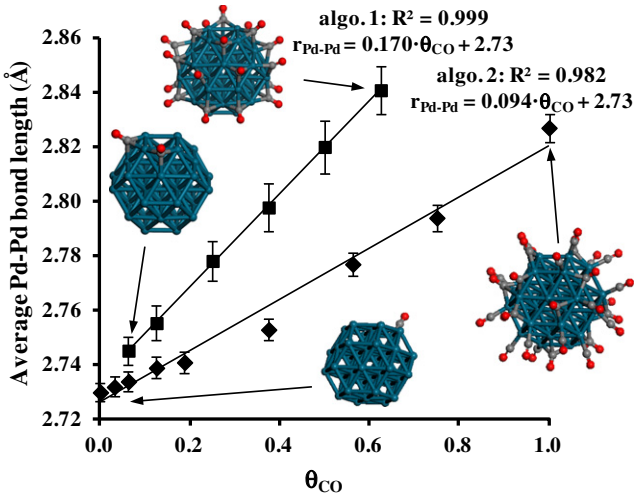

Fig. 10. Mean Pd—Pd bondlength of Pd_{38} NP as a function of CO coverage. Error bars show the standard deviation.

bonding of hollow versus linearly-bound CO, and hence larger perturbation of the underlying Pd_{38} NP framework. *Algorithms 1* and *2* predict significantly different sensitivities of $r_{<Pd—Pd>}$ to θ_{CO}, providing an avenue for experimentally testing whether CO adsorption commences via all hollow (*algorithm 1*) or mixed adsorption (*algorithm 2*) structures via e.g. coverage dependent EXAFS, one of the few techniques able to precisely measure interatomic distances of sub-2 nm NPs under reactive environments. This observation may also explain the low population of the hollow site usually seen experimentally (e.g. in the DRIFTS spectrum of Fig. 8). The Pd_{38} cluster used in our calculations is at the smaller length scale of those generally prepared experimentally, and likely exhibits greater surface flexibility than larger clusters, more readily accommodating the Pd—Pd bond expansion required for hollow site occupation.

The narrow distribution of Pd—Pd bondlengths observed for each CO coverage, evidenced by the small values of $\sigma_{<Pd—Pd>}$ in Fig. 10, strongly indicates that the Pd_{38} NP lattice expansion is isotropic. From a catalytic perspective, the implication is that variations in surface CO coverage under reaction conditions could systematically regulate isotropic expansion/contraction of palladium NPs, and hence influence molecular co-adsorption, bond activation and ultimately both activity and selectivity (as is reported for O and CO adsorption and CO dissociation over Ru(0001) [97] wherein DFT calculations of Mavrikakis et al. demonstrate an increase in surface reactivity with lattice expansion). Coverage-dependent CO DRIFTS studies would offer another means to experimentally verify our predicted lattice expansion of palladium nanoparticles, since Fig. 8 suggests that this occurs concomitant with a 63 and 29 cm^{-1} blue-shift in the respective hCO and lCO bands, with the latter a strong feature of experimental CO absorption spectra.

Conclusions

B3LYP and PBE DFT calculations have been combined to obtain information on IR spectroscopic adsorption frequencies and intensities for CO chemisorption over Pd nanoparticles as a function of particle size (i.e. Pd_4, Pd_{13} and Pd_{38}) and CO coverage. IR absorption spectra were subsequently simulated for a Pd_{38} nanoparticle, employing two computational approaches to obtain optimised $Pd_{38}CO_n$ structures. Calculated IR spectra using the B3LYP XC-functional to estimate the IR intensities, and PBE to give estimated frequencies, are in good agreement with experimental DRIFTS spectrum for CO adsorption over 2.22% Pd nanoparticles supported on a KIT-6 silica [15] provided a mixed population of hollow, bridge and atop species are included, and RAIRS and SFG studies of model Pd nanoparticle catalysts [39,86]. At low coverages ($\theta \rightarrow 0$) we find adsorption energy trends in good agreement with earlier work, and show that the dependence on particle size depends on adsorption site, with hollow and bridge sites showing adsorption energies that are more favourable on small clusters, and linear sites showing a weakening in adsorption as cluster size decreases. At high CO coverages ($\theta = 1$) linearly, bridge- and hollow-bound CO co-exist, with very small energy differences between alternative arrangements of CO molecules at different adsorption sites. Diffusion between sites is then thermally feasible at STP via a coupled diffusion process, and the equilibrium arrangement may be influenced by the additional entropy of occupying different sites. Elevated coverages of CO favour the formation of bridge-bound CO chains over a Pd_{38} nanoparticle, with some hollow-bound CO. A coverage-dependent spectroscopic blue-shift is predicted in the vibrational IR bands of adsorbed CO, coincident with an isotropic 3.5% expansion of the palladium nanoparticle framework, which could a factor in driving adsorption-induced enhancements in catalytic activity for reactions involving CO.

Author contributions

The manuscript was written through contributions of all authors.

Funding sources

We thank the EPSRC (EP/E046754/1; EP/G007594) for financial support and the award of a leadership fellowship (AFL).

Abbreviations

IR	infrared
UHV	ultra-high vacuum
DFT	density functional theory
DRIFTS	diffuse reflectance infrared Fourier-transform spectroscopy
TPD	temperature-programmed desorption
MCSCF	multi-configurational self-consistent-field
RAIRS	reflection absorption infrared spectroscopy
SCE	saturated calomel electrode
SFG	sum-frequency generation
IR-MPD	infrared multiple photon dissociation

Acknowledgment

Via our membership of the UK's HEC Materials Chemistry Consortium, which is funded by EPSRC (EP/L000202), this work used the ARCHER UK National Supercomputing Service (http://www.archer.ac.uk). We also made use of Wales' national supercomputing service provider, High Performance Computing (HPC) Wales, and the ARCCA HPC Cluster (Raven). Dr. Christopher Parlett (Aston University) is thanked for providing a DRIFT spectrum of CO adsorbed over a 2.22% Pd/KIT-6 catalyst.

Appendix A. Supplementary data

The relative energy of Pd_4(3,1) using various XC-functionals (S-Fig. 1) and the adsorption energies and vibrational frequencies for CO on Pd_{38} using PBE and B3LYP (S-Table 1) as well as the Cartesian coordinates (S-Table 2) of all optimized models are provided as supporting information. The correlation of Pd_{38} NP isotropic expansion with CO vibrational frequency is shown in S-Fig. 2. Supplementary data associated with this article can be found, in the online version, at http://dx.doi.org/10.1016/j.susc.2015.07.014.

References

[1] M.S. Chen, Y. Cal, Z. Yan, K.K. Gath, S. Axnanda, D.W. Goodman, Surf. Sci. 601 (2007) 5326.
[2] A. Haynes, Chapter 1—catalytic methanol carbonylation, in: C.G. Bruce, K. Helmut (Eds.), Advances in Catalysis, Academic Press 2010, p. 1.
[3] R. Franke, D. Selent, A. Börner, Chem. Rev. 112 (2012) 5675.
[4] R.J. Behm, K. Christmann, G. Ertl, M.A. Van Hove, J. Chem. Phys. 73 (1980) 2984.
[5] P.J. Berlowitz, C.H.F. Peden, D.W. Goodman, J. Phys. Chem. 92 (1988) 5213.
[6] T. Engel, G. Ertl, J. Chem. Phys. 69 (1978) 1267.
[7] T. Engel, G. Ertl, Adv. Catal. 28 (1979) 1.
[8] A. Logan, M.T. Paffett, J. Catal. 133 (1992) 179.
[9] H.S. Gandhi, G.W. Graham, R.W. McCabe, J. Catal. 216 (2003) 433.
[10] C.D. Zeinalipour-Yazdi, A.M. Efstathiou, J. Phys. Chem. C 112 (2008) 19030.
[11] N.P. Lebedeva, M.T.M. Koper, E. Herrero, J.M. Feliu, R.A. van Santen, J. Electroanal. Chem. 487 (2000) 37.
[12] A.C. Lausche, A.J. Medford, T.S. Khan, Y. Xu, T. Bligaard, F. Abild-Pedersen, J.K. Nørskov, F. Studt, J. Catal. 307 (2013) 275.
[13] S. Shan, V. Petkov, L. Yang, J. Luo, P. Joseph, D. Mayzel, B. Prasai, L. Wang, M. Engelhard, C.J. Zhong, J. Am. Chem. Soc. 136 (2014) 7140.
[14] A.F. Lee, C.V. Ellis, K. Wilson, N.S. Hondow, Catal. Today 157 (2010) 243.
[15] C.M.A. Parlett, D.W. Bruce, N.S. Hondow, M.A. Newton, A.F. Lee, K. Wilson, ChemCatChem 5 (2013) 939.
[16] C.D. Zeinalipour-Yazdi, R.A. van Santen, J. Phys. Chem. C 116 (2012) 8721.
[17] C.D. Zeinalipour-Yazdi, A.L. Cooksy, A.M. Efstathiou, Surf. Sci. 602 (2008) 1858.
[18] C.D. Zeinalipour-Yazdi, A.L. Cooksy, A.M. Efstathiou, J. Phys. Chem. C 111 (2007) 13872.
[19] K.A. Kacprzak, I. Czekaj, J. Mantzaras, Phys. Chem. Chem. Phys. 14 (2012) 10243.
[20] Z.-P. Liu, S.J. Jenkins, D.A. King, Phys. Rev. Lett. 94 (2005) 196102.
[21] L.M. Molina, B. Hammer, Phys. Rev. B 69 (2004) 155424.
[22] D.A.J.M. Ligthart, R.A. van Santen, E.J.M. Hensen, Angew. Chem. Int. Ed. 50 (2011) 5306.
[23] I.V. Yudanov, R. Sahnoun, K.M. Neyman, N. Rösch, J. Hoffmann, S. Schauermann, V. Johánek, H. Unterhalt, G. Rupprechter, J. Libuda, H.-J. Freund, J. Phys. Chem. B 107 (2003) 255.

[24] H. Unterhalt, G. Rupprechter, H.J. Freund, Vibrational Sum Frequency Spectroscopy on Pd (111) and Supported Pd Nanoparticles: CO Adsorption from Ultrahigh Vacuum to Atmospheric Pressure, J. Phys. Chem. B 106 (2002) 356–367.
[25] G. Rupprechter, H. Unterhalt, M. Morkel, P. Galletto, L. Hu, H.-J. Freund, Surf. Sci. 502–503 (2002) 109.
[26] T. Dellwig, G. Rupprechter, H. Unterhalt, H.-J. Freund, Phys. Rev. Lett. 85 (2000) 776.
[27] V. Fernandez, T. Giessel, O. Schaff, K.M. Schindler, A. Theobald, C.J. Hirschmugl, S. Bao, A.M. Bradshaw, C. Baddeley, A.F. Lee, R.M. Lambert, D.P. Woodruff, V. Fritzsche, Z. Phys. Chemie-Int. J. Res. Phys. Chem. Chem. Phys. 198 (1997) 73.
[28] M. Tüshaus, W. Berndt, H. Conrad, A.M. Bradshaw, B. Persson, Appl. Phys. A Mater. Sci. Process. 51 (1990) 91.
[29] J. Szanyi, D.W. Goodman, J. Phys. Chem. 98 (1994) 2972.
[30] H. Dropsch, M. Baerns, Appl. Catal. A Gen. 158 (1997) 163.
[31] J.M. Flores-Camacho, J.-H. Fischer-Wolfarth, M. Peter, C.T. Campell, S. Shauermann, H.-J. Freund, Phys. Chem. Chem. Phys. 13 (2011) 16800.
[32] J.-H. Fischer-Wolfarth, J.A. Farmer, J.M. Flores-Camacho, A. Genest, I.V. Yudanov, N. Rösch, C.T. Campbell, S. Schauermann, H.-J. Freund, Phys. Rev. B 81 (2010).
[33] P.J. Feibelman, B. Hammer, J.K. Nørskov, F. Wagner, M. Scheffler, R. Stumpf, R. Watwe, J. Dumesic, J. Phys. Chem. B 105 (2001) 4018.
[34] B. Hammer, Y. Morikawa, J.K. Nørskov, Phys. Rev. Lett. 76 (1996) 2141.
[35] V. Bertin, E. Agacino, R. López-Rendon, E. Poulain, J. Molec. Struct. THEOCHEM 796 (2006) 243.
[36] P. Sautet, M.K. Rose, J.C. Dunphy, S. Behler, M. Salmeron, Surf. Sci. 453 (2000) 25.
[37] J.A. Herron, S. Tonelli, M. Mavrikakis, Surf. Sci. 606 (2012) 1670.
[38] M.K. Rose, T. Mitsui, J. Dunphy, A. Borg, D.F. Ogletree, M. Salmeron, P. Sautet, Surf. Sci. 512 (2002) 48.
[39] M. Morkel, H. Unterhalt, T. Klüner, G. Rupprechter, H.-J. Freund, Surf. Sci. 586 (2005) 146.
[40] I.V. Yudanov, M. Metzner, A. Genest, N. Rösch, J. Phys. Chem. C 112 (2008) 20269.
[41] I.V. Yudanov, A. Genest, S. Schauermann, H.-J. Freund, N. Rösch, Nano Lett. 12 (2012) 2134.
[42] B. Zhu, G. Thrimurthulu, L. Delannoy, C. Louis, C. Mottet, J. Creuze, B. Legrand, H. Guesmi, J. Catal. 308 (2013) 272.
[43] M.J. Frisch, G.W. Trucks, H.B. Schlegel, G. E., M.A.R. Scuseria, J.R. Cheeseman, G. Scalmani, V. Barone, B. Mennucci, M.C.G.A. Petersson, R.C. Gaussian 09, Gaussian Inc, Wallingford CT, 2009.
[44] A.D. Becke, J. Chem. Phys. 98 (1993) 5648.
[45] C. Lee, W. Yang, R.G. Parr, Phys. Rev. B 37 (1988) 785.
[46] Y. Zhao, D.G. Truhlar, Theor. Chem. Accounts 120 (2008) 215.
[47] J.M. Tao, J.P. Perdew, V.N. Staroverov, G.E. Scuseria, Phys. Rev. Lett. 91 (2003) 146401.
[48] O.A. Vydrov, G.E. Scuseria, J.P. Perdew, J. Chem. Phys. 126 (2007) 154109.
[49] J.P. Perdew, K. Burke, M. Ernzerhof, Phys. Rev. Lett. 77 (1996) 3865.
[50] C. Adamo, V. Barone, J. Chem. Phys. 108 (1998) 664.
[51] W.J. Hehre, R.F. Stewart, J.A. Pople, J. Chem. Phys. 51 (1969) 2657.
[52] W.R. Wadt, P.J. Hay, J. Chem. Phys. 82 (1985) 284.
[53] T.H. Dunning Jr., P.J. Hay, Modern Theoretical Chemistry, Plenum, New York, 1976.
[54] W.J. Stevens, H. Basch, M. Krauss, J. Chem. Phys. 81 (1984) 6026.
[55] W.J. Stevens, M. Krauss, H. Basch, P.G. Jasien, Can. J. Chem. 70 (1992) 612.
[56] D.E. Woon, T.H. Dunning Jr., J. Chem. Phys. 98 (1993) 1358.
[57] A. Wilson, T. van Mourik, T.H. Dunning Jr., J. Mol. Struct. 388 (1997) 339.
[58] K.A. Peterson, D.E. Woon, T.H. Dunning Jr., J. Chem. Phys. 100 (1994) 7410.
[59] R.A. Kendall, T.H. Dunning Jr., R.J. Harrison, J. Chem. Phys. 96 (1992) 6796.
[60] T.H. Dunning Jr., J. Chem. Phys. 90 (1989) 1007.
[61] F. Weigend, F. Furche, R. Ahlrichs, J. Chem. Phys. 119 (2003) 12753.
[62] F. Weigend, R. Ahlrichs, Phys. Chem. Chem. Phys. 7 (2005) 3297.
[63] S.F. Boys, F. Bernardi, Mol. Phys. 19 (1970) 553.
[64] I.V. Yudanov, M. Metzner, A. Genest, N. Rösch, J. Phys. Chem. C 112 (2008) 20269.
[65] H.J. Monkhorst, J.D. Pack, Phys. Rev. B 13 (1976) 5188.
[66] G. Kresse, J. Furthmüller, Phys. Rev. B 54 (1996) 11169.
[67] G. Kresse, J. Hafner, Phys. Rev. B 47 (1993) 558.
[68] Y. Zhao, D.G. Truhlar, Acc. Chem. Res. 41 (2008) 157–167.
[69] G. Kresse, D. Jouber, Phys. Rev. B 59 (1999) 1758.
[70] P.E. Blöchl, Phys. Rev. B 50 (1994) 17953.
[71] J. Paier, M. Marsman, G. Kresse, J. Chem. Phys. 127 (2007) 024103.
[72] K. Mogi, Y. Sakai, T. Sonoda, Q. Xu, Y. Souma, J. Phys. Chem. A 107 (2003) 3812.
[73] P.C. Gravelle, Adv. Catal. 22 (1972) 191.
[74] P.C. Gravelle, Catal. Rev. Sci. Eng. 16 (1977) 37.
[75] R. Trebbe, R. Goddard, A. Rufińska, K. Seevogel, K.-R. Pörschke, Organometallics 18 (1999) 2466.
[76] J.T. Yates, T.M. Duncan, S.D. Worley, R.W. Vaughan, J. Chem. Phys. 70 (1979) 1219.
[77] H.C. Yao, W.G. Rothschild, J. Chem. Phys. 68 (1978) 4774.
[78] G. Zanti, D. Peeters, Eur. J. Inorg. Chem. 3904–3911 (2009).
[79] D. Dai, K. Balasubramanian, Chem. Phys. 103 (1995) 648.
[80] G. Blyholder, J. Phys. Chem. 68 (1964) 2772.
[81] P. Gruene, A. Fielicke, G. Meijer, D.M. Rayner, Phys. Chem. Chem. Phys. 10 (2008) 6144.
[82] K. Luo, T. Wei, C.W. Yi, S. Axnanda, D.W. Goodman, J. Phys. Chem. B 109 (2005) 23517.
[83] M.A. Vannice, S.Y. Wang, J. Phys. Chem. 85 (1981) 2543.
[84] T. Komeda, Y. Kim, M. Kawai, Surf. Sci. 502–503 (2002) 12.
[85] K.L. Wong, B.V. Rao, G. Pawin, E. Ulin-Avila, L. Bartels, J. Chem. Phys. 123 (2005) 201102.
[86] K. Wolter, O. Seiferth, H. Kuhlenbeck, M. Baumer, H.-J. Freund, Surf. Sci. 399 (1998) 190.
[87] M. Peter, S. Adamovsky, J.M. Flores Camacho, S. Schauermann, Faraday Discuss. 162 (2013) 341.
[88] H. Unterhalt, G. Rupprechter, H.-J. Freund, J. Phys. Chem. B 106 (2001) 356.
[89] S. Bertarione, D. Scarano, A. Zecchina, V. Johánek, J. Hoffmann, S. Schauermann, M.M. Frank, J. Libuda, G. Rupprechter, H.-J. Freund, J. Phys. Chem. B 108 (2004) 3603.
[90] T. Lear, R. Marshall, E.K. Gibson, T. Schutt, T.M. Klapotke, G. Rupprechter, H.-J. Freund, J.M. Winfield, D. Lennon, Phys. Chem. Chem. Phys. 7 (2005) 565.
[91] M. Scheffler, Surf. Sci. 81 (1979) 562.
[92] W.K. Kuhn, J. Szanyi, D.W. Goodman, Surf. Sci. Lett. 274 (1992) L611.
[93] S. Zou, I. Villegas, C. Stuhlmann, M.J. Weaver, Electrochim. Acta 43 (1998) 2811.
[94] P.S. Bagus, C.J. Nelin, C.W. Bauschlicher, Phys. Rev. B 28 (1983) 5423.
[95] T.O. Menteş, N. Stojić, N. Binggeli, M.A. Niño, A. Locatelli, L. Aballe, M. Kiskinova, E. Bauer, Phys. Rev. B 77 (2008) 155414.
[96] V. Kumar, Y. Kawazoe, Phys. Rev. B 66 (2002) 144413.
[97] M. Mavrikakis, B. Hammer, J.K. Nørskov, Phys. Rev. Lett. 81 (1998) 2819.